Druckfreigabe/approval for printing

Without corrections/ ohne Korrekturen ☐

After corrections/ nach Ausführung der Korrekturen ☐

Date/Datum: .....

Signature/Zeichen: .....

10
Coatings on High Aspect Ratio Structures

Jeffrey W. Elam

10.1
Introduction

Atomic layer deposition (ALD) utilizes self-limiting chemical reactions to achieve atomic-level control over film thickness and composition without the need for line-of-site access to the precursor source required for most other deposition techniques [1, 2]. Consequently, ALD allows complex surface features such as deep trenches and narrow pores to be coated with great precision. This capability benefits a remarkably broad range of applications, some of which have been realized and many others that are currently topics of active research.

Since this chapter is devoted to ALD coatings on high aspect ratio structures, it is helpful to define what is meant by aspect ratio. Any topographical surface feature such as a trench or pore can be characterized by a dimensionless aspect ratio. In the case of a rectangular trench, the aspect ratio is given by the trench depth divided by the trench width. Likewise, the aspect ratio of a cylindrical pore that is open on one end is equal to the length of the pore divided by the pore diameter. A thin film that has a uniform thickness on all surfaces of a coated object is called "conformal." ALD excels at producing conformal coatings on high aspect ratio features. This capability provides a straightforward means for imparting the desired chemical properties (e.g., surface acidity, corrosion resistance, catalytic activity, etc.) or physical properties (e.g., hardness, optical reflectivity, coefficient of friction, electrical resistance, etc.) to nearly any surface. In this way, the three-dimensional shape of an object can be decoupled from the surface properties of the object. Consequently, one has the freedom to select a convenient template with the desired shape, porosity, or structure without worrying about the physical or chemical properties of the template because these traits can be tuned later by applying ALD layers. This versatility is made even more powerful when applied to nanoscale materials, and currently ALD is being utilized to synthesize nanostructured materials for a diverse range of technologies [3].

Some of the most vexing problems facing society today relate to energy. The future of our economy and climate depend upon developing new means for producing,

UNCORRECTED PROOF

Atomic Layer Deposition of Nanostructured Materials, First Edition. Edited by Nicola Pinna and Mato Knez.
© 2012 Wiley-VCH Verlag GmbH & Co. KGaA. Published 2012 by Wiley-VCH Verlag GmbH & Co. KGaA.

storing, and conserving energy in renewable and economically viable ways. Solutions to these problems are likely to result from revolutionary rather than incremental changes in technology, and nanomaterials with tunable structure, porosity, and composition hold tremendous promise in this respect [4]. For this reason, the topic of ALD coatings on high aspect ratio structures is more than purely academic. An appreciation and understanding of this subject, particularly by practitioners in energy disciplines that may be new to ALD, could lead to the breakthroughs in materials synthesis necessary to solve our energy problems.

This chapter will survey the field of ALD as it applies to the coating of high aspect ratio structures. In the first section, we will introduce several mathematical models that are useful for understanding ALD in porous structures and for predicting the necessary exposure conditions required to achieve conformal coverage. Next, we will review some of the analytical characterization techniques used to evaluate the degree of conformality or infiltration of ALD coatings in high aspect ratio structures. After this, we will give examples to illustrate ALD at high aspect ratios and the technological applications that they address. These examples will be presented in the order of increasing aspect ratio: 10, 100, 1000, and beyond. Next, we will describe some nonideal situations in which limitations in the coating process or violations of the simplifying assumptions made in the models lead to nonconformal films. Finally, we will summarize and briefly touch on the future of ALD in high aspect ratio structures.

10.2 Models and Analysis

A fundamental question when coating high aspect ratio structures by ALD is: "How long must the exposure times be?" The answer to this question depends on the particular conditions used that will dictate the coating regime. In the case of a very high surface area substrate coated in a relatively small ALD reactor, nearly all of the precursor will be consumed immediately upon entering the reactor and the coating process will be limited by the rate of precursor delivery. In this transport-limited regime, the exposure time is independent of the particular nanostructure of the support and can be calculated by dividing the number of sites to be coated by the rate of introduction of precursor molecules into the ALD reactor. In the reaction-limited regime, the ALD surface reactions are exceedingly slow and the precursor supply is constant and abundant. In this regime, the nanostructure of the support is inconsequential and the exposure time can be calculated from the Langmuir adsorption model. However, most cases of interest occur in the diffusion-limited regime where both the ALD reaction rate and the precursor supply are sufficiently high. In the diffusion-limited regime, the exposure time required to achieve saturation increases as the square of the aspect ratio. The following models apply to the diffusion-limited regime, but a criterion will be given for differentiating between the reaction- and diffusion-limited cases.

UNCORRECTED PROOF

10.2.1
Analytical Method

Gordon analytically derived an expression to calculate the saturation exposure time based on gas conductance equations [5]. This derivation assumes Knudsen diffusion of the ALD precursors, which means that gas-phase collisions between molecules can be ignored. Knudsen diffusion requires that the mean free path of the precursor molecule, λ, is much larger than the characteristic feature size such as the pore diameter, d. For instance, consider trimethylaluminum (TMA) in a 50 nm pore under a nitrogen pressure of 1 Torr at 177 °C. In this case, $\lambda \sim 50$ and $\lambda \gg d$, so Knudsen diffusion applies. For Knudsen diffusion conditions, Gordon derives the following quantity:

$$t = S(2\pi mkT)^{1/2}/P[1 + (19/4)a + 3/2a^2], \tag{10.1}$$

where P is the pressure (Pa), t is the time (s), S is the saturation coverage of the molecule in question (molecules/m^2), m is the mass of the precursor (kg), k is the Boltzmann constant (J/K), T is the temperature (K), and a is the aspect ratio of the pore. The quantity $S(2\pi mkT)^{1/2}/P$ is the exposure time required to reach saturation on a planar substrate assuming a reactive sticking coefficient of 1. For very large aspect ratios, the a^2 term in Eq. (10.1) dominates, so the exposure time increases as the square of the aspect ratio. This model provides a simple analytical expression for the exposure time but makes a number of simplifying assumptions that are sometimes violated in practical situations. For instance, this analysis assumes a reactive sticking coefficient of 1 and neglects the effect of coverage on sticking coefficient (i.e., Langmuir adsorption). Furthermore, this model assumes that the aspect ratio of the pore does not change during the coating process.

Improvements on this model have been made in which the expressions for coverage as a function of exposure time and depth into a surface feature were allowed to depend on the sticking coefficient and the surface coverage [6, 7]. The primary difference between these methods and the Gordon method is that the coverage profiles obtained exhibited a more gradual transition between saturation coverage and zero coverage as the sticking coefficient decreased. In other words, for slower ALD surface reactions (lower initial sticking probability), the thickness profiles become broadened.

10.2.2
Monte Carlo Simulations

Elam used Monte Carlo simulations to analyze ALD in nanopores and derived an expression for the saturating exposure time [8]. This method also assumed Knudsen diffusion, and furthermore that the ALD metal precursor (e.g., TMA) was the limiting reagent. However, this simulation explicitly included the sticking coefficient and also accounted for pore shrinkage during coating so that the effective aspect ratio changed during the deposition. To simulate Knudsen diffusion, a particle was allowed to "hop"

UNCORRECTED PROOF

a distance d, equal to the local pore diameter, randomly either into or out of the pore. The Monte Carlo simulations yielded the following expression for the minimum exposure time:

$$t = 9.2 \times 10^{-7}\left(\sqrt{m}Na^2\right)/P, \tag{10.2}$$

where N is the density of ALD reactive sites (sites/cm^2), m is the molecular mass of the metal precursor (amu), and P is the partial pressure of the metal precursor (Torr). The original study used a different definition for the aspect ratio, so the constant term in Eq. (10.2) has been adjusted for consistency with Eq. (10.1). In the limit of a thin ALD coating and a high sticking coefficient, Eq. (10.2) can be shown to be equivalent to Eq. (10.1).

To differentiate between the reaction- and diffusion-limited regimes, Elam defined the hopping coefficient, $H = 16/a^2$, as the fraction of hops that reach an empty site in the pore. The hopping confident can then be compared with the reactive sticking coefficient, S. In the diffusion-limited regime, $S \gg H$ and the surface sites along each pore fill up sequentially in order from the pore entrance. In the reaction-limited regime, $H \gg S$ and the precursor molecules essentially equilibrate along the pore axis before reaction occurs. Consequently, the surface sites fill up uniformly along each pore. Both Eqs. (10.1) and (10.2) apply to the diffusion-limited regime, which is the most typical situation for ALD in high aspect ratio structures.

10.3 Characterization Methods for ALD Coatings in High Aspect Ratio Structures

The analytical methods described above are very useful for predicting the necessary partial pressures and exposure times required to achieve self-limiting, saturating growth in high aspect ratio structures. But to validate these models, it is necessary to have reliable methods for quantifying the degree of infiltration of the ALD materials. A wide variety of characterization methods have been developed to accomplish this objective. Although some of these methods apply equally well to thin films on both porous and planar supports, other techniques are useful only for porous materials because they rely on the tremendous surface area afforded by high aspect ratio nanoporous materials. For instance, the infiltration of a nanoporous template by an optically absorbing material such as a metal can often be confirmed by eye after a single ALD cycle. Similarly, visual inspection under an optical microscope of cross-sectional specimens of a high surface area support such as silica gel or nanoporous extrudate can reveal the extent of infiltration of even submonolayer ALD coatings. Simple weight gain measurements are very effective for quantifying the saturation ALD conditions or for determining the ALD growth rate in nanoporous media [9, 10].

Electron microscopy is another very useful technique for characterizing ALD coatings in high aspect ratio structures. Transmission electron microscopy (TEM) is used very often to evaluate the conformality of ALD coatings in high aspect ratio trench structures [11]. Typically, this method requires the careful preparation of

UNCORRECTED PROOF

cross-sectional specimens using ion milling or a focused ion beam (FIB). However, a simpler method has been developed in which nanoporous anodic aluminum oxide (AAO) is infiltrated by ALD and the alumina is dissolved to facilitate TEM analysis of the resulting nanotubes [12]. Cross-sectional scanning electron microscopy (SEM) can also be quite revealing. However, this technique requires destroying the sample to expose a cross-sectional view. While the resolution of SEM (~1–10 nm) is typically lower than that of TEM (~0.1–1 nm), it has the advantage of allowing a wider range of view to facilitate the analysis of larger specimens such as entire 100 μm silica gel beads coated by ALD [9].

Because aspect ratio is a dimensionless quantity, the analysis of ALD films in macroscopic pores or features can be used for understanding ALD in microscopic pores. For instance, one useful and convenient technique for evaluating ALD in trenches is to fabricate an "artificial trench" by clamping two pieces of silicon together separated by a thin metal foil to define a precise gap. The thickness of an ALD coating can then be evaluated as a function of distance into the "trench" using macroscopic measurement techniques such as ellipsometry allowing a direct comparison with models [7]. Another strategy used glass capillaries with an inside diameter of 20 μm and a length of 2 mm to evaluate ALD conformality at high aspect ratios. Following WN ALD, the capillaries were examined under an optical microscope to determine the extent of infiltration [13].

A variety of methods exist that provide element-specific information about the spatial distribution of ALD materials in high aspect ratio materials. For instance, TEM and SEM can be equipped with energy- or wavelength-dispersive X-ray detectors (e.g., EDAX) to image the spatial distribution of different elements in ALD-coated nanomaterials [10]. Rutherford backscattering spectroscopy (RBS) is commonly used to evaluate the elemental composition of thin films on planar substrates as a function of depth into the film. However, this technique has also been used with great success to evaluate the degree of infusion of ALD thin films into porous templates such as porous silicon [14] and TiO_2 nanoparticle films [15]. Secondary ion mass spectrometry (SIMS) is another element-specific analytical technique that has been utilized to analyze cross-sectional specimens of high aspect ratio materials coated by ALD including aerogels [14, 16].

The methods described above are all performed *ex situ* so that the information is obtained only after the film is deposited. However, a variety of *in situ* analytical methods have been utilized to analyze ALD films in porous materials during the coating process. For example, Fourier transform infrared (FTIR) spectroscopy has been used to examine the infiltration of ALD Al_2O_3 and SiO_2 in high aspect ratio AAO membranes [8]. FTIR has also been used extensively to evaluate ALD processes in samples comprised of pressed nanopowders [17]. The quartz crystal microbalance (QCM) is another *in situ* characterization tool that has been utilized to explore ALD in high aspect ratio substrates. In these experiments, a film of colloidal semiconducting nanocrystals (quantum dots) was prepared on the surface of the QCM sensor. The mass gain per ZnO ALD cycle observed by QCM for the quantum dot film was 13 × larger than the corresponding mass gain on an uncoated sensor, and provided a quantitative measure of the internal surface area of the film [18]. Finally, quadrupole

UNCORRECTED PROOF

mass spectrometry (QMS) has been used to elucidate the infiltration of high aspect ratio nanoporous silica gel [9]. In these experiments, the QMS could resolve subtle changes in the surface chemistry as a function of the ALD Al_2O_3 film thickness in addition to establishing the necessary exposure conditions to achieve saturation.

10.4 Examples of ALD in High Aspect Ratio Structures

The following examples of ALD coatings in high aspect ratio supports are intended to illustrate the unique capabilities of ALD for coating porous materials. We will present these examples in the order of increasing aspect ratio.

10.4.1 Aspect Ratio of 10

10.4.1.1 Trenches

The classic example of a high aspect ratio structure is a micromachined trench in single-crystal silicon. Silicon trenches are ubiquitous in the microelectronics industry. For instance, ALD coatings of high dielectric constant materials are used in dynamic random access memory [19]. Trenches are also commonly used during ALD process development as a convenient substrate for assaying the conformality of the coating. In such cases, the wafer is typically cleaved to reveal a cross section for examination by SEM. For example, Figure 10.1 shows an SEM image of an ALD copper sulfide (Cu_2S) film prepared in a trench ~1 μm wide with an aspect ratio of 9 [20]. As shown by the magnified insets, the 45 nm thick Cu_2S film has the same

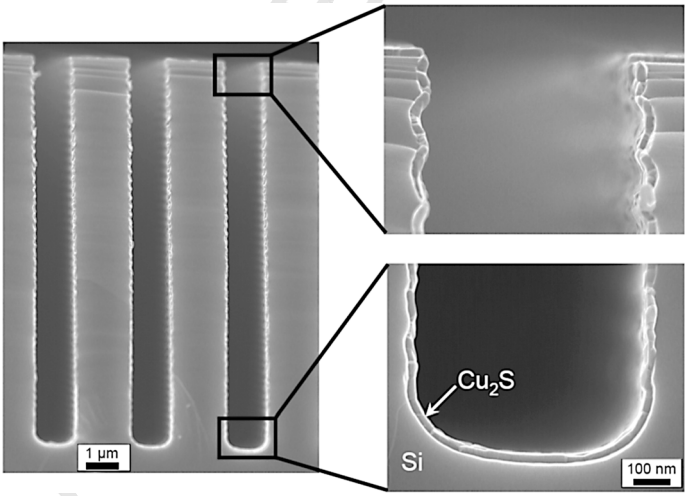

Figure 10.1 Cross-sectional SEM images of 45 nm ALD Cu_2S film on silicon trench structure. Reprinted with permission from Ref. [20]. Copyright 2009, the American Institute of Physics.

UNCORRECTED PROOF

thickness on the top and bottom of the trench and therefore exhibits high conformality.

10.4.1.2 MEMS

Another example of ALD films in structures with aspect ratio of order 10 is microelectromechanical systems (MEMS). MEMS devices consist of micromachined structures, typically comprised of silicon, with dimensions on the micron scale designed to act as resonators, mirrors, actuators, motors, and so on. A common problem encountered in MEMS devices is stiction, a phenomenon whereby adjacent moving parts become permanently bonded due to hydrophobic, electrostatic, or other forces. Another problem is friction and wear between moving parts. These problems can be alleviated by coating all surfaces with antistiction [21], lubricating [22], or wear-resistant coatings [23], and ALD is an attractive means for accomplishing this. Figure 10.2 shows SEM images of a MEMS cantilever that has been coated using ALD Al_2O_3 and subsequently cut using a focused ion beam to reveal a cross section [24]. The gap between the cantilever beam and the underlying contact pad is 1 μm, and the half-width of the beam is 25 μm yielding an aspect ratio of 25. The lower SEM image

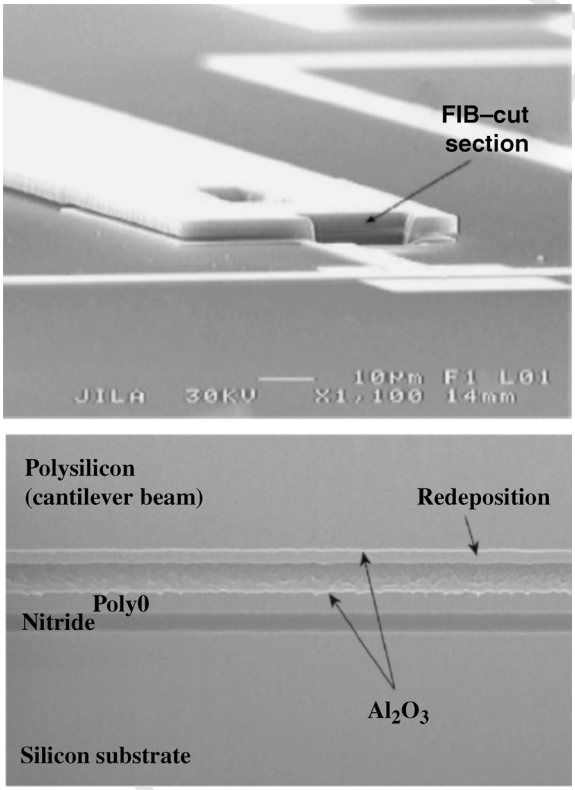

Figure 10.2 Cross-sectional SEM images of FIB-cut MEMS cantilever coated with 60 nm ALD Al_2O_3. Reprinted with permission from Ref. [24]. Copyright 2003, Elsevier.

UNCORRECTED PROOF

demonstrates that the Al_2O_3 coating extends uniformly over all exposed surfaces inside of this narrow gap.

10.4.2 Aspect Ratio of 100

10.4.2.1 Anodic Aluminum Oxide

AAO is a common platform for synthesizing nanostructured materials by ALD. AAO is made by the simultaneous electrochemical oxidation and etching of aluminum metal in an acid solution and results in the formation of nanometer-sized, circular pores arranged in a hexagonal close-packed arrangement that extend into the aluminum oxide perpendicular to the surface (Figure 10.3). The AAO can be left bonded to the aluminum substrate, or it can be removed and further processed to form freestanding membranes in which the pores are accessible from both sides. A typical pore diameter of 50 nm and a membrane thickness of 25 μm yield an aspect ratio of 250. AAO membranes have been coated by ALD with a wide variety of materials including metal oxides [8, 25], metal nitrides [26, 27], and metals [28–30]. In some cases, the AAO template can be subsequently dissolved yielding nanotubes of the ALD coating [31]. Track etched polycarbonate membranes have a similar nanostructure and have also been used as a template for fabricating nanotubes by ALD [32].

AAO membranes provide a convenient scaffold for synthesizing functional nanostructured materials by ALD for use in applications such as photovoltaics [33], catalysis [34], and magnetic devices [28]. In addition, the regular geometry and high aspect ratio make AAO an excellent substrate for evaluating ALD conformality and

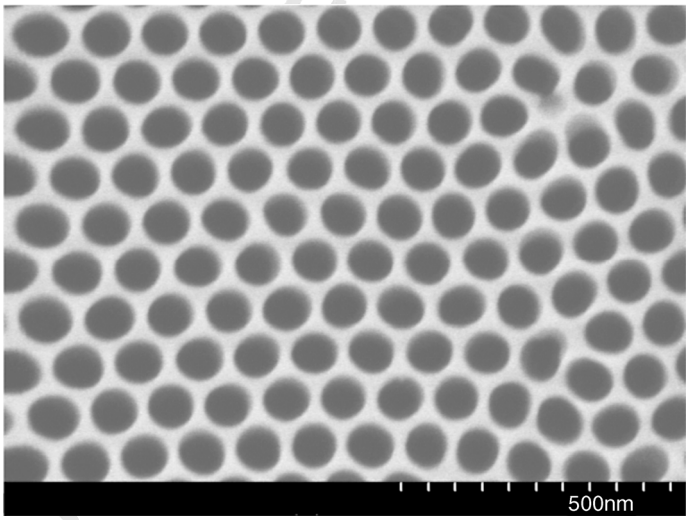

Figure 10.3 SEM image of AAO membrane surface showing hexagonal arrangement of $d = 75$ nm nanopores. Reprinted with permission from J.W. Elam, unpublished.

UNCORRECTED PROOF

for testing infiltration models. In one such investigation, freestanding AAO samples were coated with ALD ZnO and the exposure times for the ALD ZnO precursors were varied [8]. Cross-sectional specimens of the coated AAO were examined using EDAX to determine the spatial location of the Zn. Figure 10.4a demonstrates that as the exposure times increased, the ZnO migrated progressively further into the AAO membrane. This behavior is quantified in Figure 10.4b in which the two-dimensional Zn maps of Figure 10.4a were integrated to show line scans. These results were in excellent quantitative agreement with Monte Carlo simulations of the ALD infiltration process. Figure 10.4c shows the integration of the areas under the curves in Figure 10.4b and demonstrates that the ALD ZnO growth in the AAO nanopores follows the expected $t^{1/2}$ time dependence. Furthermore, the exposure times in Figure 10.4c are in good quantitative agreement with Eqs. (10.1) and (10.2).

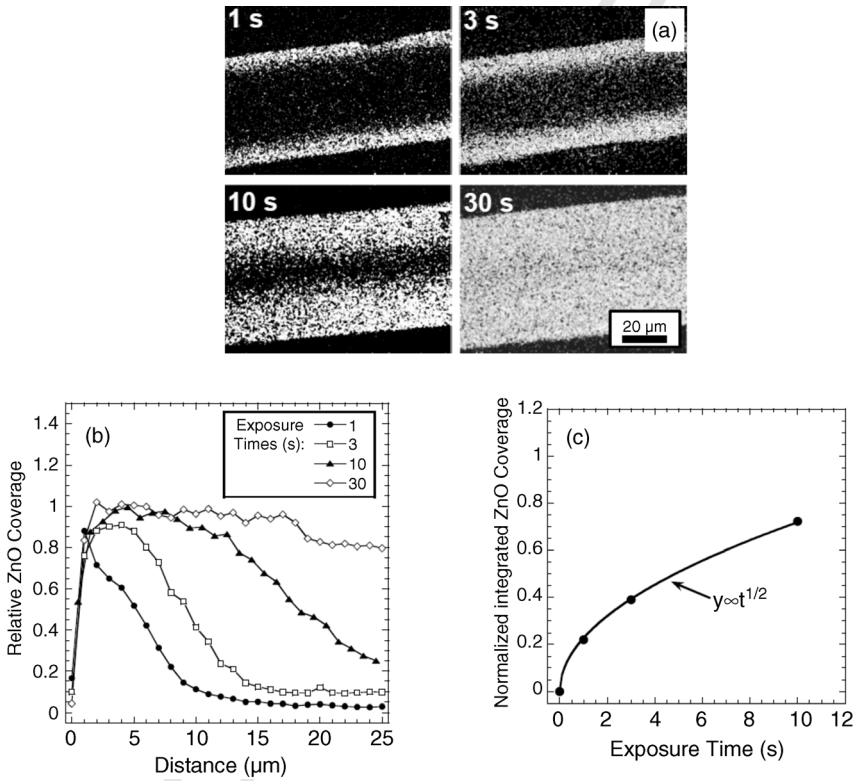

Figure 10.4 (a) Cross-sectional EDAX images of Zn concentration of AAO membranes coated with ZnO ALD films using precursor exposures times of 1, 3, 10, and 30 s. (b) Line scan profiles of Zn coverage versus distance into AAO membrane generated by integrating the EDAX images in (a). (c) Normalized ZnO coverage versus precursor exposure time calculated by integrating the line scan profiles in (b) demonstrating the $t^{1/2}$ functional dependence of the ZnO infiltration. Reprinted with permission from Ref. [8]. Copyright 2003, the American Chemical Society.

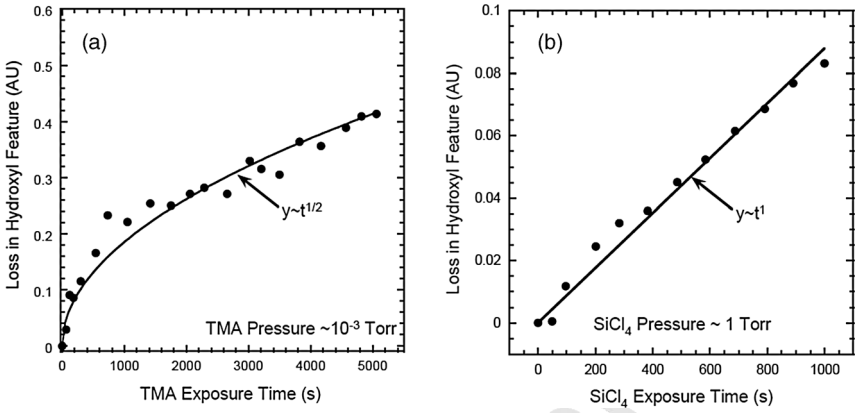

Figure 10.5 (a) Loss in surface hydroxyl concentration versus TMA exposure time during Al_2O_3 ALD measured using *in situ* FTIR. The $t^{1/2}$ functional dependence is characteristic of a diffusion-limited process. (b) *In situ* FTIR measurements of surface hydroxyl loss during SiO_2 ALD versus $SiCl_4$ exposure, where the $t^{1/2}$ functional form signals a reaction-limited process. Reprinted with permission from Ref. [8]. Copyright 2003, the American Chemical Society.

The same study described above also explore the different infiltration behaviors for Al_2O_3 and SiO_2 ALD in AAO corresponding to the diffusion- and reaction-limited regimes explained in Section 10.2.2 [8]. During the TMA exposures for Al_2O_3 ALD, hydroxyl groups are consumed as the TMA chemisorbs to the surface. By monitoring the decrease in the OH intensity using FTIR, the extent of the TMA reaction was determined. Figure 10.5a plots the hydroxyl loss as a function of TMA exposure time in a high aspect ratio AAO membrane. In this case, the sticking coefficient, S, for the TMA chemisorption is $\sim 10^{-2}$, while the hopping coefficient $H = 16/a^2 \sim 10^{-5}$. Since $S \gg H$, the process is diffusion limited so that the reactive sites in each AAO pore fill up in order and the $t^{1/2}$ time dependence is observed. In contrast, Figure 10.5b shows a similar measurement of the $SiCl_4$ adsorption during SiO_2 ALD and exhibits a linear dependence of coverage versus exposure time. In this case, $S \sim 10^{-9}$, so $S \ll H$ meaning the process is reaction limited so that the reactive sites in the pores fill up uniformly versus time.

The fact that the reactive sites in the AAO pores fill up in order in the diffusion-limited case facilitates a technique known as "stripe coating" in which ALD can be used to deposit materials selectively at specific depth locations in the AAO pores [35]. In this process, a masking exposure is performed prior to each ALD cycle in order to render the sites near the ends of the nanopores nonreactive to the ALD metal precursor such as diethylzinc for ZnO ALD. For instance, if the AAO is first exposed to a subsaturating TMA exposure, then each pore will be methyl-terminated to a pore depth determined by the duration of the TMA exposure. During the subsequent DEZ exposure, these sites will be nonreactive so that the DEZ will only chemisorb deeper down the pores. The duration of the DEZ exposure then determines the width of the resulting ZnO "stripe." After the DEZ exposure, the sample is exposed to H_2O to repopulate the surface with hydroxyl groups so that the TMA–DEZ–H_2O exposures

UNCORRECTED PROOF

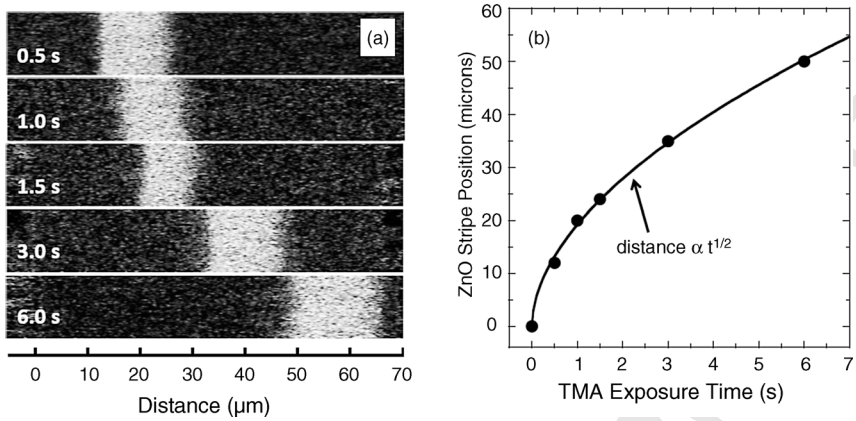

Figure 10.6 (a) Cross-sectional EDAX maps of Zn concentration following ZnO stripe coating in AAO using a TMA/DEZ/H_2O dosing sequence and varying only the TMA exposure time. (b) Position of trailing edge of ZnO stripes in (a) versus TMA exposure time demonstrating the $t^{1/2}$ dependence expected for this diffusion-limited infiltration process. Reprinted with permission from Ref. [35]. Copyright 2007, the American Institute of Physics.

can be repeated. Figure 10.6a shows two-dimensional EDAX maps of the spatial distribution of Zn for polished cross sections of AAO membranes prepared using TMA masking exposures of increasing exposure time. As seen in this figure, the stripes move progressively farther into the AAO pores for longer TMA exposure times. The position of the trailing edge of the ZnO stripe is plotted in Figure 10.6b versus the TMA exposure time, and exhibits the $t^{1/2}$ time dependence characteristic of this diffusion-limited coating process.

10.4.2.2 Inverse Opals

Inverse opals represent another class of high aspect ratio materials that have been fabricated successfully by ALD infiltration (see Chapter 15). In one example, a suspension of monodisperse silica nanospheres with a diameter of 400 nm was cast on a planar substrate to generate a film with a thickness of 10 μm in which the nanospheres formed a face-centered cubic lattice [36]. The resulting gap between the spheres was ~60 μm yielding an initial aspect ratio of 175. The opal was then infiltrated by TiO_2 ALD, and the silica spheres were subsequently removed by etching in hydrofluoric acid leaving behind the inverse opal structure in Figure 10.7a. Reflectivity spectra recorded for a series of such materials with increasing TiO_2 thickness exhibit a smooth and continuous variation in the location of a peak in the reflectance spectrum known as the pseudophotonic band gap. It is interesting to note that as the ALD TiO_2 thickness increased, the gaps narrowed and gradually closed down so that the aspect ratio increased greatly. Nevertheless, the highly conformal TiO_2 ALD process allowed for a nearly complete filling of the voids leaving behind only small air pockets (Figure 10.7b). Inverse opals have been fabricated in this way for a variety of ALD materials including ZnO [37], WN [38], GaAs [39], and ZnS [40], as well as multilayers of different materials [41].

UNCORRECTED PROOF

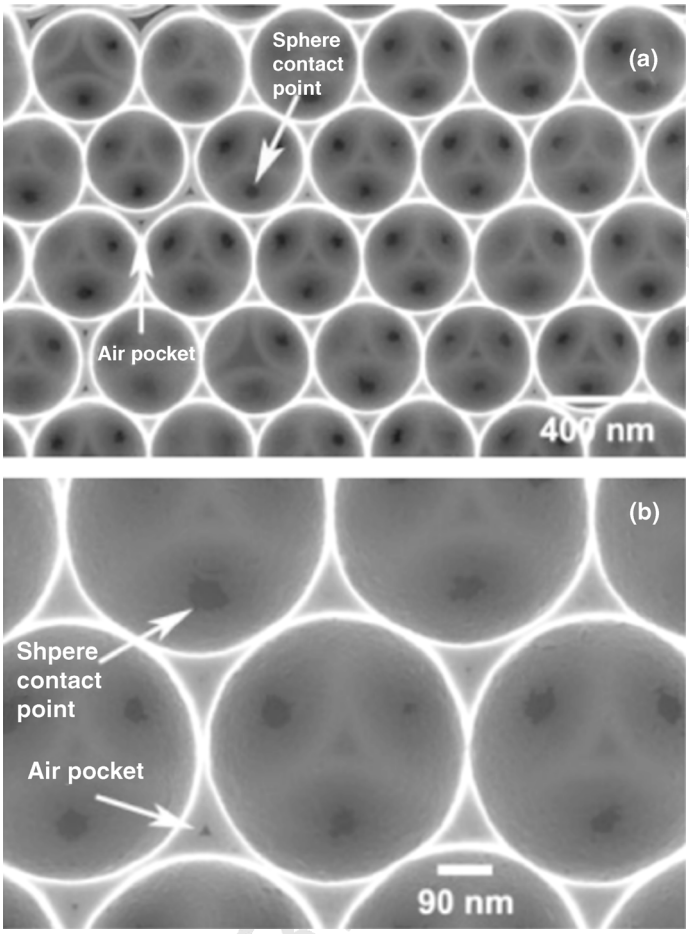

Figure 10.7 SEM images of cross sections of 433 nm ALD TiO_2 inverse opals prepared by FIB to expose the (111) surface. Reprinted with permission from Ref. [36]. Copyright 2005, Wiley.

10.4.3 Aspect Ratio of 1000 and Beyond

10.4.3.1 Silica gel

Silica gel is a granular, mesoporous material that is widely utilized as a support material for heterogeneous catalysts because of its very high specific surface area (50–500 m^2/g). A typical silica gel particle has a radius of 50 μm and a pore size of 30 nm yielding an aspect ratio of ~1600. In a previous study exploring Al_2O_3 ALD on this challenging substrate [9], a series of 1 g specimens were treated using three ALD cycles and the weight changes were recorded as the TMA exposure time was varied (Figure 10.8). Saturation was observed for TMA exposures of ~60 s demonstrating self-limiting behavior even on this high aspect ratio, high surface area support. *In situ*

UNCORRECTED PROOF

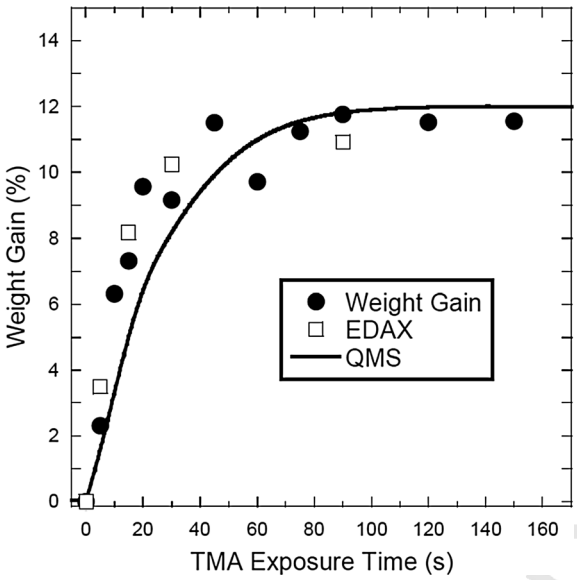

Figure 10.8 Measurements of ALD Al_2O_3 infiltration of silica gel versus TMA exposure time obtained from weight gain measurements (solid circles), EDAX measurements (open squares), and integrated QMS measurements (solid line). Reprinted with permission from Ref. [9]. Copyright 2010, Elsevier.

quadrupole mass spectrometry (QMS) was used to monitor the CH_4 produced during the TMA exposures (Figure 10.8). The temporal behavior of the QMS CH_4 signal agreed well with the weight gain measurements proving that QMS can accurately probe ALD processes in porous media. The weight gain and Al content as determined by EDAX measurements increased linearly with ALD cycles for Al_2O_3 film thicknesses of up to 2.4 nm. These findings were consistent with layer-by-layer growth where the silica gel pores remained open and the surface area stayed relatively constant as expected for conformal growth in the 30 nm pores.

To gain more insight into the Al_2O_3 ALD process on the silica gel, cross-sectional specimens of individual silica gel beads were prepared and examined using EDAX measurements of the Al concentration for various TMA exposure times (Figure 10.9).

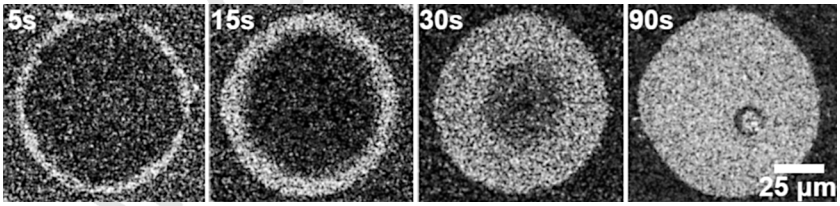

Figure 10.9 EDAX elemental maps for Al obtained from polished cross sections of silica gel following Al_2O_3 ALD using TMA exposure times of 5, 15, 30, and 90 s. Reprinted with permission from Ref. [9]. Copyright 2010, Elsevier.

UNCORRECTED PROOF

The Al_2O_3 ALD infiltrated progressively from the outside toward the middle with increasing TMA exposure times. Recall that a similar behavior was observed for the diffusion-limited ZnO ALD in AAO membranes (Figure 10.4a). In this case, the diffusion-limited regime was confirmed by plotting the integrated Zn coverage against the DEZ exposure time and observing a $t^{1/2}$ dependence (Figure 10.4c). Al coverages were obtained for the silica gel by radially integrating the two-dimensional Al EDAX profiles and using an r^3 weighting factor, where r is the radial distance from the center of the silica gel particle. These data are plotted as the open squares in Figure 10.8. The EDAX measurements agree with the direct weight gain measurements, and both data sets exhibit a linear dependence of the Al coverage with TMA exposure time for coverages below ~10 wt%, where the Al_2O_3 ALD is below saturation. This linear dependence contradicts the anticipated $t^{1/2}$ dependence expected for a diffusion-limited process. However, in these experiments the very high surface area of the silica gel forced the process to be in the transport-limited regime and consequently the Al coverage varied linearly with exposure time [9].

10.4.3.2 **Aerogels**

Aerogels are another form of high surface area, high aspect ratio solid and can be manufactured from a variety of materials including silica, carbon, and titania [42, 43]. For instance, silica aerogels are fabricated by the supercritical drying of a silica sol–gel and consist of a randomly interconnected network of fine filaments and particles. The silica sol–gel can be spin or dip coated onto a planar substrate to produce a thin film aerogel or cast to form an aerogel monolith. The ability to coat ultralow-density silica aerogels with conformal layers of different materials using ALD can benefit technologies such as gas sensing, catalysis, and photovoltaics [16, 44–49].

Aerogels can have extremely high aspect ratios. For instance, one study examined ALD ZnO on monolithic silica aerogel specimens with a thickness $t = 1$ mm and a pore size $d = 30$ nm yielding an aspect ratio $t/(2d) \sim 17\,000$ [47]. The silica aerogels had an open, filamentous structure and SEM images revealed that and the conformal ZnO coatings increased the filament diameter with increasing number of ALD ZnO cycles (Figure 10.10). Curiously, both the ZnO weight gain and the Zn content inferred from EDAX measurements increased quadratically versus the number of ZnO ALD cycles (Figure 10.11). This finding is surprising given the highly linear ALD ZnO growth observed on flat substrates. This discrepancy is explained by the linear increase in filament diameter with ZnO cycles (Figure 10.10) since the amount of ZnO deposited per cycle varies with the square of the filament diameter. This behavior is in contrast to the linear increase in mass with increasing ALD cycles observed on silica gel [9]. However, in the silica gel example, the 2.4 nm ALD Al_2O_3 coating was smaller than the 30 nm silica gel primary particles so that the surface area remained nearly constant. But in the silica aerogel study, the 12 nm ZnO coating was much larger than the ~2 nm silica aerogel filaments causing the surface area to change dramatically.

A different study explored W ALD in carbon aerogels for use as spallation targets in rare isotope facilities [50]. In these experiments, carbon aerogel monoliths were cut into 1 mm thick slabs comprised of an interconnected network of 10 nm filaments

UNCORRECTED PROOF

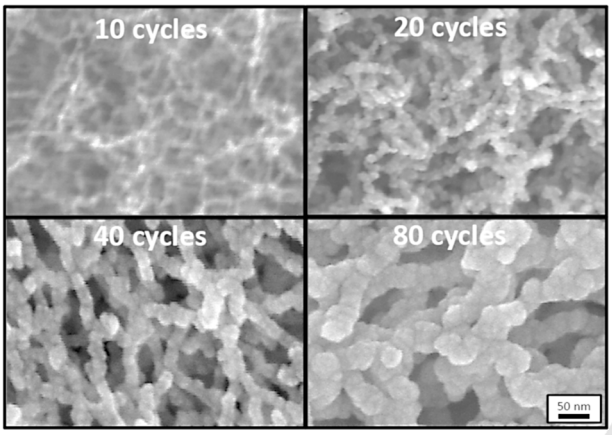

Figure 10.10 SEM images of silica aerogel versus ZnO ALD cycles illustrating progressive thickening of aerogel filaments. Reprinted with permission from Ref. [47]. Copyright 2006, J.W. Elam *et al.*

separated by 10 nm gaps defining an aspect ratio of $\sim 10^5$. The aerogel mass was found to increase quadratically after 3 cycles and then saturated beyond ~10 cycles (Figure 10.12). In contrast, companion measurements performed on planar witness samples showed a linear increase in W thickness following a three-cycle nucleation period. This quadratic behavior is similar to ZnO ALD on silica aerogel [47], which

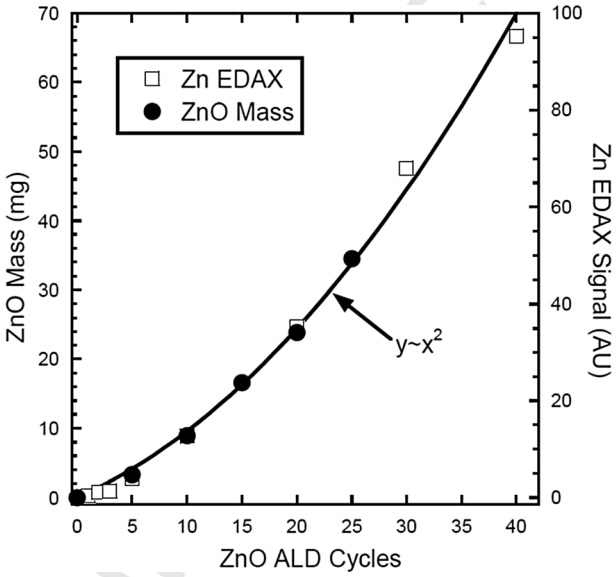

Figure 10.11 Mass gain and Zn EDAX signal versus ZnO ALD cycles on silica aerogel. Quadratic behavior results from linear increase in aerogel filament diameter with number of ZnO cycles. Reprinted with permission from Ref. [47]. Copyright 2006, J.W. Elam *et al.*

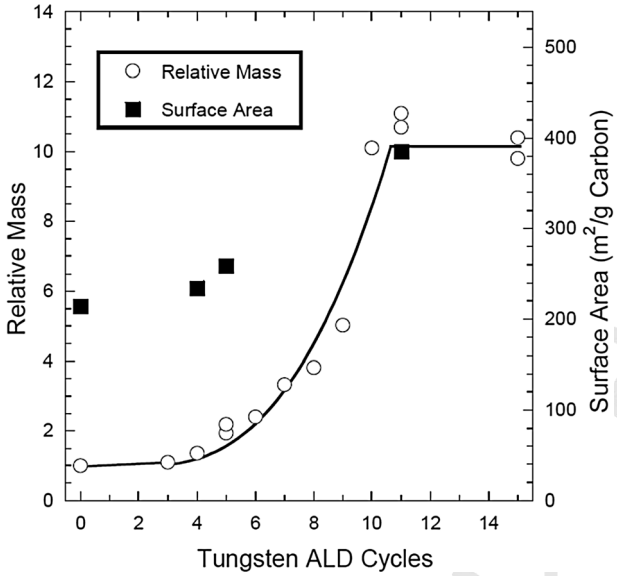

Figure 10.12 Relative mass and surface area of W-coated carbon aerogel versus number of ALD W cycles. Reprinted with permission from Ref. [50]. Copyright 2006, the American Institute of Physics.

resulted from an increase in aerogel filament diameter with ALD film thickness. In support of this mechanism, both the carbon aerogel surface area measured using nitrogen adsorption (Figure 10.12) and the filament diameter determined from TEM images (Figure 10.13) were found to increase with ALD W thickness. The saturation in aerogel mass beyond 10 ALD W cycles resulted from filling the 10 nm gaps with the ~5 nm thick ALD W films.

10.5
Nonideal Behavior during ALD in High Aspect Ratios

As described above, ALD excels at coating high aspect ratio materials. Nevertheless, there are instances where this method fails to produce conformal coatings as desired or where the thickness profile deviates significantly from that predicted by the models and it is worthwhile to review some of these examples of nonideal behavior. Roughly speaking, these examples can be divided into two categories: physical and chemical. One example of a physical nonideality leading to bad conformality is pore closure. If the ALD film thickness exceeds half the width or diameter of the pore, then the surface feature will become closed or clogged and this will prevent transport of the precursor vapors deeper into the pores [50]. In the case of a perfectly conformal coating in a uniform feature, closure will occur essentially simultaneously throughout the depth of the feature forming a solid plug and this tendency can be exploited to engineer nanomaterials [51]. Deliberate subsaturating ALD exposures can be used to seal the outer surfaces of a porous, low-*k* dielectric material prior to depositing a

UNCORRECTED PROOF

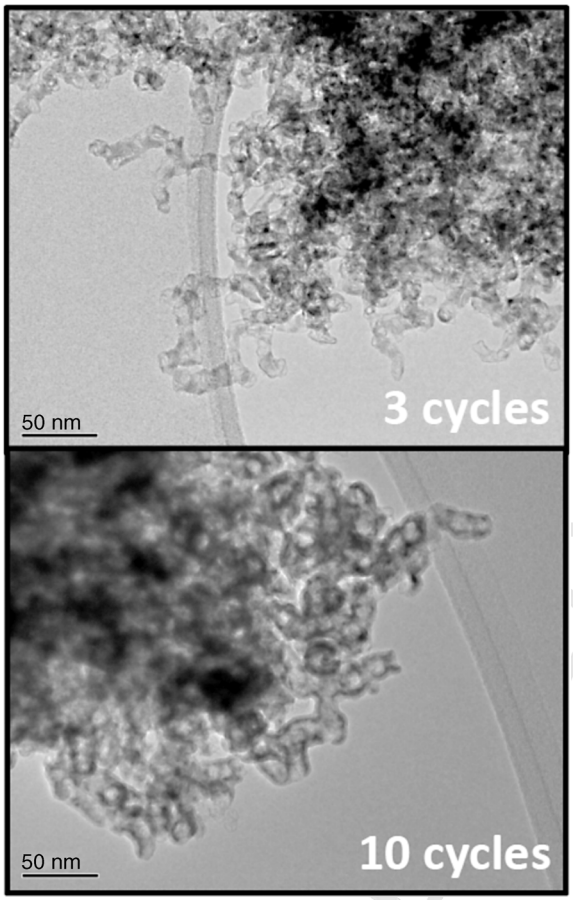

Figure 10.13 TEM images of carbon aerogel following three and seven cycles of W ALD. Reprinted with permission from Ref. [50]. Copyright 2006, the American Institute of Physics.

copper diffusion barrier such as ALD WN. This will prevent the ALD WN from infiltrating the low-*k* material and causing electrical shorts or increasing the dielectric constant [52]. Plasma treatment can also be used to densify and activate the exterior surfaces of the low-*k* material to facilitate intentional pore closure [53].

Another example of a physical nonideality during ALD in high aspect ratios is the precursor depletion (Section 10.2). Existing models for ALD in high aspect ratio structures assume that the precursor partial pressure remains constant so that saturation times can be predicted from Knudsen diffusion [5, 8]. But in the limit of a very high substrate surface area, the precursor is rapidly consumed through chemisorption on the reactive sites and the coating process will be transport limited. Conformal coatings can still be obtained if sufficient precursor is delivered to titrate all of the reactive sites, and the saturation exposure time will be independent of the aspect ratio and the reactive sticking coefficient [9].

UNCORRECTED PROOF

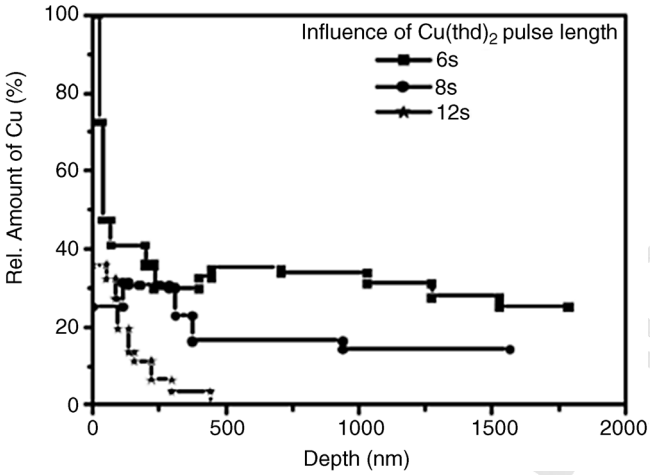

Figure 10.14 Influence of the $Cu(thd)_2$ pulse time on the infiltration depth of ALD Cu_2S in a TiO_2 matrix consisting of 25 nm particles as determined by RBS measurements. Reprinted with permission from Ref. [15]. Copyright 2004, the American Chemical Society.

Thermal decomposition is one example of a chemical nonideality that limits the uniformity of ALD films. Conformal ALD in high aspect ratios requires that the probability for thermal decomposition of the precursors must be negligible compared to the probability for diffusing to an empty site and compared to the reactive sticking coefficient. In one study of Cu_2S ALD in a 4 μm porous film comprised of TiO_2 nanoparticles with sizes of 9–50 nm, RBS depth profile measurements yielded very nonuniform Cu thickness profiles (Figure 10.14) [15]. These experiments used alternating exposures to $Cu(thd)_2$ and H_2S at a temperature of 200 °C and the researchers found that as the $Cu(thd)_2$ exposure time was increased, the Cu_2S infiltration depth actually decreased. This behavior was attributed to thermal decomposition of the $Cu(thd)_2$ precursor and subsequent clogging of the TiO_2 nanopores.

The thermal decomposition of O_3 can reduce conformality during the ALD of metal oxides. Since some oxides will catalyze O_3 decomposition, the O_3 loss rate is highly dependent on both the temperature and composition of the substrate surface. For example, nonuniform thickness profiles generated during the ALD of In_2O_3 using cyclopentadienyl indium and O_3 were attributed to the catalytic destruction of the O_3 on the ALD In_2O_3 surface [54]. Nevertheless, reasonably uniform ALD ITO coatings could be prepared in high aspect ratio AAO membranes using this method by extending the O_3 exposure times to compensate for the reduced O_3 concentrations [55]. Similarly, the surface recombination of radicals such as O and H in plasma-enhanced ALD can profoundly affect the conformality of ALD films in high aspect ratio structures. As with O_3 decomposition, radical recombination is highly surface dependent so that film conformality will depend greatly on the material being deposited as well as the surface species involved [56].

UNCORRECTED PROOF

Another chemical nonideality that can affect the conformality of ALD films is etching. Halogenated precursors such as $NbCl_5$ can react with metal oxide films to form volatile oxychloride species. This process can etch the surface to the point of complete removal of the film [57]. This problem will be particularly acute during ALD in porous supports where very large metal chloride exposures are needed. Metal chloride precursors can also form large, micron-sized agglomerates as a result of gaseous diffusion of hydroxychlorides and subsequent redeposition [58]. Another nonideality is blocking of adsorption sites by the gaseous by-product formed on neighboring sites. For instance, the HCl by-product of the $TiCl_4/H_2O$ process for TiO_2 ALD can readsorb onto the TiO_2 surface and prevent the adsorption and reaction of additional $TiCl_4$ molecules [59]. This problem is not unique to halogenated compounds since the isopropanol product of the $Ti(O^iPr)_4/H_2O$ process can also bind strongly to TiO_2 and limit additional $Ti(O^iPr)_4$ adsorption [60]. These phenomena will lead to nonconformal films in high aspect ratio substrates because the by-products generated on the outer regions of the pores will adsorb deeper within the pores and prevent or inhibit growth on these inner regions.

Nonideal behavior was observed during the ALD of Cu and Cu_3N films in aerogel substrates [61]. In these studies, the penetration depth of the films was found to be nearly independent of the precursor exposure time in complete contradiction of the expected diffusion-limited behavior. The authors postulated that this behavior resulted from thermal decomposition of the amidinate precursor, possibly catalyzed by metal nanoparticles, or from site blocking by the reaction by-products.

10.6 Conclusions and Future Outlook

One of the most useful attributes of ALD as it relates to nanomaterials synthesis is the capability to apply precise, conformal coatings on very high aspect ratio features including trenches, pores, and powders. This capability allows the surface properties to be tuned independently of surface structure and greatly expands the list of potential applications for ALD technology. Both analytical and numerical descriptions for the infiltration of high aspect ratio features during ALD provide useful descriptions and allow saturation conditions to be determined. This chapter has reviewed examples of ALD coatings on high aspect ratio substrates ranging from micromachined trenches with aspect ratios of $\sim$10 to aerogels with aspect ratios of 10^5. We expect that future developments will expand the list of available ALD materials for coating porous and high aspect ratio templates and also identify new, promising applications for this methodology. Continued growth in this field will require developing new processes and new precursors to overcome some of the nonidealities that are sometimes encountered, such as surface-catalyzed thermal decomposition. Due to the unique capability of ALD to apply conformal films on high aspect ratio structures, it is likely that this technology will play a central role in areas such as photovoltaics and batteries and help establish a new economy based on clean, renewable energy.

UNCORRECTED PROOF

References

1. Ritala, M. and Leskelä, M. (2001) Atomic layer deposition, in *Handbook of Thin Film Materials*, vol. 1 (ed. H.S. Nalwa), Academic Press, San Diego, CA, pp. 103.
2. George, S.M. (2010) Atomic layer deposition: an overview. *Chem. Rev.*, **110** (1), 111–131.
3. Knez, M., Niesch, K., and Niinisto, L. (2007) Synthesis and surface engineering of complex nanostructures by atomic layer deposition. *Adv. Mater.*, **19** (21), 3425–3438.
4. Rolison, D.R., Long, R.W., Lytle, J.C., Fischer, A.E., Rhodes, C.P., McEvoy, T.M., Bourga, M.E., and Lubers, A.M. (2009) Multifunctional 3D nanoarchitectures for energy storage and conversion. *Chem. Soc. Rev.*, **38** (1), 226–252.
5. Gordon, R.G., Hausmann, D., Kim, E., and Shepard, J. (2003) A kinetic model for step coverage by atomic layer deposition in narrow holes or trenches. *Chem. Vapor Depos.*, **9** (2), 73–78.
6. Kim, J.Y., Ahn, J.H., Kang, S.W., and Kim, J.H. (2007) Step coverage modeling of thin films in atomic layer deposition. *J. Appl. Phys.*, **101** (7), 0735021–0735023.
7. Dendooven, J., Deduytsche, D., Musschoot, J., Vanmeirhaeghe, R.L., and Detavernier, C. (2009) Modeling the conformality of atomic layer deposition: the effect of sticking probability. *J. Electrochem. Soc.*, **156** (4), P63–P67.
8. Elam, J.W., Routkevitch, D., Mardilovich, P.P., and George, S.M. (2003) Conformal coating on ultrahigh-aspect-ratio nanopores of anodic alumina by atomic layer deposition. *Chem. Mater.*, **15** (18), 3507–3517.
9. Elam, J.W., Libera, J.A., Huynh, T.H., Feng, H., and Pellin, M.J. (2010) Atomic layer deposition of aluminum oxide in mesoporous silica gel. *J. Phys. Chem. C*, **114**, 17286–17292.
10. Libera, J.A., Elam, J.W., and Pellin, M.J. (2008) Conformal ZnO coatings on high surface area silica gel using atomic layer deposition. *Thin Solid Films*, **516** (18), 6158–6166.
11. Sneh, O., Clark-Phelps, R.B., Londergan, A.R., Winkler, J., and Seidel, T.E. (2002) Thin film atomic layer deposition equipment for semiconductor processing. *Thin Solid Films*, **402** (1–2), 248–261.
12. Perez, I., Robertson, E., Banerjee, P., Henn-Lecordier, L., Son, S.J., Lee, S.B., and Rubloff, G.W. (2008) TEM-based metrology for HfO_2 layers and nanotubes formed in anodic aluminum oxide nanopore structures. *Small*, **4** (8), 1223–1232.
13. Becker, J.S., Suh, S., Wang, S.L., and Gordon, R.G. (2003) Highly conformal thin films of tungsten nitride prepared by atomic layer deposition from a novel precursor. *Chem. Mater.*, **15** (15), 2969–2976.
14. Ducso, C., Khanh, N.Q., Horvath, Z., Barsony, I., Utriainen, M., Lehto, S., Nieminen, M., and Niinisto, L. (1996) Deposition of tin oxide into porous silicon by atomic layer epitaxy. *J. Electrochem. Soc.*, **143** (2), 683–687.
15. Reijnen, L., Feddes, B., Vredenberg, A.M., Schoonman, J., and Goossens, A. (2004) Rutherford backscattering spectroscopy study of $TiO_2/Cu_{1.8}S$ nanocomposites obtained by atomic layer deposition. *J. Phys. Chem. B*, **108** (26), 9133–9137.
16. Baumann, T.F., Biener, J., Wang, Y.M.M., Kucheyev, S.O., Nelson, E.J., Satcher, J.H., Elam, J.W., Pellin, M.J., and Hamza, A.V. (2006) Atomic layer deposition of uniform metal coatings on highly porous aerogel substrates. *Chem. Mater.*, **18** (26), 6106–6108.
17. Ferguson, J.D., Weimer, A.W., and George, S.M. (2000) ALD of Al_2O_3 and SiO_2 on BN particles using sequential surface reactions. *Appl. Surf. Sci.*, **162–163**, 280–292.
18. Pourret, A., Guyot-Sionnest, P., and Elam, J.W. (2009) Atomic layer deposition of ZnO in quantum dot thin films. *Adv. Mater.*, **21** (2), 232–235.
19. Gerritsen, E., Emonet, N., Caillat, C., Jourdan, N., Piazza, M., Fraboulet, D., Boeck, B., Berthelot, A., Smith, S., and Mazoyer, P. (2005) Evolution of materials technology for stacked-capacitors in 65 nm embedded-DRAM. *Solid-State Electron.*, **49** (11), 1767–1775.

UNCORRECTED PROOF

20 Martinson, A.B.F., Elam, J.W., and Pellin, M.J. (2009) Atomic layer deposition of Cu_2S for future application in photovoltaics. *Appl. Phys. Lett.*, **94** (12), 1231071–1231073.

21 Herrmann, C.F., Delrio, F.W., Bright, V.M., and George, S.M. (2005) Conformal hydrophobic coatings prepared using atomic layer deposition seed layers and non-chlorinated hydrophobic precursors. *J. Micromech. Microeng.*, **15** (5), 984–992.

22 Scharf, T.W., Prasad, S.V., Dugger, M.T., Kotula, P.G., Goeke, R.S., and Grubbs, R.K. (2006) Growth, structure, and tribological behavior of atomic layer-deposited tungsten disulphide solid lubricant coatings with applications to MEMS. *Acta Mater.*, **54** (18), 4731–4743.

23 Mayer, T.M., Elam, J.W., George, S.M., Kotula, P.G., and Goeke, R.S. (2003) Atomic-layer deposition of wear-resistant coatings for microelectromechanical devices. *Appl. Phys. Lett.*, **82** (17), 2883–2885.

24 Hoivik, N.D., Elam, J.W., Linderman, R.J., Bright, V.M., George, S.M., and Lee, Y.C. (2003) Atomic layer deposited protective coatings for micro-electromechanical systems. *Sens. Actuators A*, **103** (1–2), 100–108.

25 Bae, C., Yoo, H., Kim, S., Lee, K., Kim, J., Sung, M.A., and Shin, H. (2008) Template-directed synthesis of oxide nanotubes: fabrication, characterization, and applications. *Chem. Mater.*, **20** (3), 756–767.

26 Banerjee, P., Perez, I., Henn-Lecordier, L., Lee, S.B., and Rubloff, G.W. (2009) Nanotubular metal–insulator–metal capacitor arrays for energy storage. *Nat. Nanotechnol.*, **4** (5), 292–296.

27 Miikkulainen, V., Suvanto, M., and Pakkanen, T.A. (2008) Molybdenum nitride nanotubes. *Thin Solid Films*, **516** (18), 6041–6047.

28 Daub, M., Knez, M., Goesele, U., and Nielsch, K. (2007) Ferromagnetic nanotubes by atomic layer deposition in anodic alumina membranes. *J. Appl. Phys.*, **101** (9), 09J1111–09J1113.

29 Comstock, D.J., Christensen, S.T., Elam, J.W., Pellin, M.J., and Hersam, M.C. (2010) Tuning the composition and nanostructure of Pt/Ir films via anodized aluminum oxide templated atomic layer deposition. *Adv. Funct. Mater.*, **20**, 3099–3105.

30 Kim, W.H., Park, S.J., Son, J.Y., and Kim, H. (2008) Ru nanostructure fabrication using an anodic aluminum oxide nanotemplate and highly conformal Ru atomic layer deposition. *Nanotechnology*, **19** (4), 1–8.

31 Lee, M., Kim, T., Bae, C., Shin, H., and Kim, J. (2010) Fabrication and applications of metal-oxide nano-tubes. *JOM*, **62** (4), 44–49.

32 Shin, H.J., Jeong, D.K., Lee, J.G., Sung, M.M., and Kim, J.Y. (2004) Formation of TiO_2 and ZrO_2 nanotubes using atomic layer deposition with ultraprecise control of the wall thickness. *Adv. Mater.*, **16** (14), 1197–1200.

33 Martinson, A.B.F., Elam, J.W., Hupp, J.T., and Pellin, M.J. (2007) ZnO nanotube based dye-sensitized solar cells. *Nano Lett.*, **7** (8), 2183–2187.

34 Stair, P.C., Marshall, C., Xiong, G., Feng, H., Pellin, M.J., Elam, J.W., Curtiss, L., Iton, L., Kung, H., Kung, M., and Wang, H.H. (2006) Novel, uniform nanostructured catalytic membranes. *Top. Catal.*, **39** (3–4), 181–186.

35 Elam, J.W., Libera, J.A., Pellin, M.J., and Stair, P.C. (2007) Spatially controlled atomic layer deposition in porous materials. *Appl. Phys. Lett.*, **91** (24), 2431051–2431053.

36 King, J.S., Graugnard, E., and Summers, C.J. (2005) TiO_2 inverse opals fabricated using low-temperature atomic layer deposition. *Adv. Mater.*, **17** (8), 1010–1013.

37 Scharrer, M., Wu, X., Yamilov, A., Cao, H., and Chang, R.P.H. (2005) Fabrication of inverted opal ZnO photonic crystals by atomic layer deposition. *Appl. Phys. Lett.*, **86** (15), 1511131–1511133.

38 Rugge, A., Becker, J.S., Gordon, R.G., and Tolbert, S.H. (2003) Tungsten nitride inverse opals by atomic layer deposition. *Nano Lett.*, **3** (9), 1293–1297.

39 Povey, I.M., Whitehead, D., Thomas, K., Pemble, M.E., Bardosova, M., and Renard, J. (2006) Photonic crystal thin films of GaAs prepared by atomic layer deposition. *Appl. Phys. Lett.*, **89** (10), 1041031–1041033.

UNCORRECTED PROOF

40 King, J.S., Neff, C.W., Summers, C.J., Park, W., Blomquist, S., Forsythe, E., and Morton, D. (2003) High-filling-fraction inverted ZnS opals fabricated by atomic layer deposition. *Appl. Phys. Lett.*, **83** (13), 2566–2568.

41 King, J.S., Graugnard, E., and Summers, C.J. (2006) Photoluminescence modification by high-order photonic bands in TiO_2/ZnS: Mn multilayer inverse opals. *Appl. Phys. Lett.*, **88** (8), 0811091–0811093.

42 Baumann, T.F., Gash, A.E., Fox, G.A., Satcher, J.J.H., and Hrubesh, L.W. (2002) Oxidic aerogels, in *Handbook of Porous Solids* (eds F. Schuth, K.S.W. Sing, and J. Weitkamp), Wiley-VCH Verlag GmbH, Weinheim.

43 Rolison, D.R. (2003) Catalytic nanoarchitectures: the importance of nothing and the unimportance of periodicity. *Science*, **299** (5613), 1698–1701.

44 Kucheyev, S.O., Biener, J., Wang, Y.M., Baumann, T.F., Wu, K.J., van Buuren, T., Hamza, A.V., Satcher, J.H., Elam, J.W., and Pellin, M.J. (2005) Atomic layer deposition of ZnO on ultralow-density nanoporous silica aerogel monoliths. *Appl. Phys. Lett.*, **86** (8), 0831081–0831083.

45 Biener, J., Baumann, T.F., Wang, Y.M., Nelson, E.J., Kucheyev, S.O., Hamza, A.V., Kemell, M., Ritala, M., and Leskelä, M. (2007) Ruthenium/aerogel nanocomposites via atomic layer deposition. *Nanotechnology*, **18** (5), 1–4.

46 King, J.S., Wittstock, A., Biener, J., Kucheyev, S.O., Wang, Y.M., Baumann, T.F., Giri, S.K., Hamza, A.V., Baeumer, M., and Bent, S.F. (2008) Ultralow loading Pt nanocatalysts prepared by atomic layer deposition on carbon aerogels. *Nano Lett.*, **8** (8), 2405–2409.

47 Elam, J.W., Xiong, G., Han, C.Y., Wang, H.H., Birrell, J.P., Welp, U., Hryn, J.N., Pellin, M.J., Baumann, T.F., Poco, J.F., and Satcher, J.H. (2006) Atomic layer deposition for the conformal coating of nanoporous materials. *J. Nanomater.*, 1–5.

48 Hamann, T.W., Martinson, A.B.E., Elam, J.W., Pellin, M.J., and Hupp, J.T. (2008) Aerogel templated ZnO dye-sensitized solar cells. *Adv. Mater.*, **20** (8), 1560–1564.

49 Hamann, T.W., Martinson, A.B.F., Elam, J.W., Pellin, M.J., and Hupp, J.T. (2008) Atomic layer deposition of TiO_2 on aerogel templates: new photoanodes for dye-sensitized solar cells. *J. Phys. Chem. C*, **112** (27), 10303–10307.

50 Elam, J.W., Libera, J.A., Pellin, M.J., Zinovev, A.V., Greene, J.P., and Nolen, J.A. (2006) Atomic layer deposition of W on nanoporous carbon aerogels. *Appl. Phys. Lett.*, **89** (5), 0531241–0531243.

51 Wang, J.J., Deng, X.G., Varghese, R., Nikolov, A., Sciortino, P., Liu, F., Chen, L., and Liu, X.M. (2005) Filling high aspect-ratio nano-structures by atomic layer deposition and its applications in nano-optic devices and integrations. *J. Vac. Sci. Technol. B*, **23** (6), 3209–3213.

52 de Rouffignac, P., Li, Z.W., and Gordon, R.G. (2004) Sealing porous low-*k* dielectrics with silica. *Electrochem. Solid-State Lett.*, **7** (12), G306–G308.

53 Travaly, Y., Schuhmacher, J., Baklanov, M.R., Giangrandi, S., Richard, O., Brijs, B., Van Hove, M., Maex, K., Abell, T., Somers, K.R.F., Hendrickx, M.F.A., Vanquickenborne, L.G., Ceulemans, A., and Jonas, A.M. (2005) A theoretical and experimental study of atomic-layer-deposited films onto porous dielectric substrates. *J. Appl. Phys.*, **98** (8), 0835151–0835159.

54 Elam, J.W., Martinson, A.B.F., Pellin, M.J., and Hupp, J.T. (2006) Atomic layer deposition of In_2O_3 using cyclopentadienyl indium: a new synthetic route to transparent conducting oxide films. *Chem. Mater.*, **18** (15), 3571–3578.

55 Martinson, A.B.F., Elam, J.W., Liu, J., Pellin, M.J., Marks, T.J., and Hupp, J.T. (2008) Radial electron collection in dye-sensitized solar cells. *Nano Lett.*, **8** (9), 2862–2866.

56 Knoops, H.C.M., Langereis, E., van de Sanden, M.C.M., and Kessels, W.M.M. (2020) Conformality of plasma-assisted ALD: physical processes and modeling. *J. Electrochem. Soc.*, **157** (12), G241–G249.

57 Elers, K.-E., Ritala, M., Leskelä, M., and Rauhala, E. (1994) $NbCl_5$ as a precursor for ALE. *Appl. Surf. Sci.*, **82/83**, 468–474.

58 Puurunen, R.L. (2005) Formation of metal oxide particles in atomic layer deposition during the chemisorption of metal chlorides: a review. *Chem. Vapor Depos.*, **11** (2), 79–90.

UNCORRECTED PROOF

59 Ritala, M., Leskelä, M., Nykanen, E., Soininen, P., and Niinisto, L. (1993) Growth of titanium dioxide thin films by atomic layer epitaxy. *Thin Solid Films*, **225**, 288–295.

60 Ritala, M., Leskelä, M., Niinisto, L., and Haussalo, P. (1993) Titanium isopropoxide as a precursor in atomic layer epitaxy of titanium-dioxide thin-films. *Chem. Mater.*, **5** (8), 1174–1181.

61 Kucheyev, S.O., Biener, J., Baumann, T.F., Wang, Y.M., Hamza, A.V., Li, Z., Lee, D.K., and Gordon, R.G. (2008) Mechanisms of atomic layer deposition on substrates with ultrahigh aspect ratios. *Langmuir*, **24** (3), 943–948.

UNCORRECTED PROOF

Keywords/Abstract

Dear Author,

Keywords and abstracts will not be included in the print version of your chapter but only in the online version.

Please check and/or supply keywords. If you supplied an abstract with the manuscript, please check the typeset version.

If you did not provide an abstract, the section headings will be displayed instead of an abstract text in the online version.

Keywords: aerogels; ALD coatings; aspect ratio; inverse opals; Knudsen diffusion; trenches. Q1

UNCORRECTED PROOF

Author Query

1. Please check the suggested keywords.

UNCORRECTED PROOF